Nanoscale

Accepted Manuscript

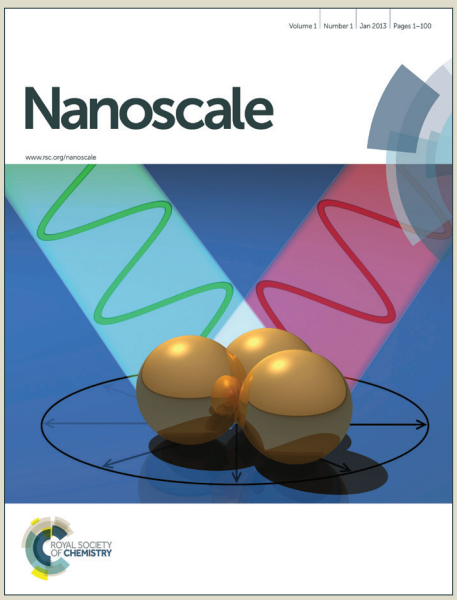

ROYAL SOCIETY OF CHEMISTRY

www.rsc.org/nanoscale

Journal Name

RSCPublishing

ARTICLE

Exploring the Benefits of Electron Tomography to Characterize the Precise Morphology of Core Shell Au@Ag Nanoparticles and its Implications for their Plasmonic Properties

Cite this: DOI: 10.1039/x0xx00000x

Received 00th January 2012,
Accepted 00th January 2012

DOI: 10.1039/x0xx00000x

www.rsc.org/

J. C. Hernández-Garrido,[a]* M. S. Moreno,[b] C. Ducati,[c] L. A. Pérez,[d] P.A. Midgley[c] and E. A. Coronado[d]*

In the design and engineering of functional core-shell nanostructures, materials characterization at small length scales remains one of the major challenges. Here we show how electron tomography in high-angle annular dark-field scanning transmission electron microscopy (HAADF-STEM) mode can be applied successfully to perform nano-metrological characterization of Au@Ag core-shell nanostructures. This work stresses the benefits of HAADF-STEM tomography and its use as a novel and rigorous tool for understanding the physical-chemical properties of complex 3D core-shell nanostructures. The reconstructed Au@Ag core-shell architecture was used as input for Discrete Dipole Approximation (DDA)-based electrodynamics simulations of the optical properties of the nanostructures. The implications for localized surface plasmon spectroscopy as well as in Raman-enhanced spectroscopies are analysed.

Introduction

Bimetallic nanoparticles have received great attention recently owing to their enhanced optical, electronic and catalytic properties which cannot be obtained for the single components nanoparticles. [1-7] Among these bimetallic system, core-shell nanostructures, formed by either the modification of nanoparticles through deposition of a thin surface layer of a different material or the formation of the shell by cation exchange, have become important routes to the preparation of functional nanomaterials. Core-shell structures allow tuning and tailoring of physical and chemical properties of the nanoparticles through chemical composition and by controlling the radius ratio of the core and the shell.[2, 8] Indeed, the physicochemical properties of the core–shell nanoparticles may be very different to those of the two constituent metals and alloyed nanoparticles.[9] Previously there has been particular interest in the optical properties that core-shell nanoparticles display due to the presence of a dielectric or semiconducting core coated with a metallic shell in which the strong optical resonance is dependent on the relative thickness of the nanoparticle core and its metallic shell.[8] Au core-Ag shell nanoparticles, denoted as Au@Ag, have attracted considerable interest: both metals display well-defined surface plasmon absorption bands (around 400 and 520 nm for Ag and Au, respectively) and they have the same fcc crystal structures with similar lattice constants: Au 0.4079 nm and Ag 0.4086 nm. As a consequence, alloyed nanoparticles can be obtained over the whole composition range. Extensive synthesis studies on bimetallic nanoparticle to form core-shell nanostructures have been performed during the recent years and are described in the excellent review by Liz-Marzán[9] and, thus, are not discussed here.

The strong dependency of the optical properties on composition, shape and size of Au@Ag nanoparticles [10-12] demands methodologies for accurate characterization at the nano scale. Transmission electron microscopy (TEM) and related electron spectroscopy techniques provide direct methods for both structural and chemical characterization of nanoparticles with sub-nanometer resolution.

Conventional and high resolution TEM in combination with electron diffraction are all commonly used to determine the shape, size and crystallinity of nanoparticles and core-shell systems.[13-16] For a more quantitative approach to structural imaging on the nanoscale, the incoherent nature of high-angle

annular dark field (HAADF) scanning-transmission electron microscopy (STEM), provides images whose intensity is approximately proportional to Z^2, (Z-contrast imaging), and to the projected thickness.[17, 18] The simple interpretability of this contrast is a great advantage in cases where identification of two phases with similar structure but different atomic number, like the present case, is needed.[19]

Although these electron microscopy techniques provide high-spatial resolution and compositionally sensitive imaging, they only enable a 2D "projection" to be made of a 3D object. Thus, in general, such images do not allow for an unambiguous measurement of size, morphology and especially the interface defining the core-shell structure. The 3D nature of this complex and heterogeneous nanostructure requires a 3D imaging technique.

Electron tomography, and its applications in materials science, has developed rapidly over recent years enabling a full 3D analysis for nanostructures. [20-22] Compared to other techniques commonly used for the characterization of core-shell nanostructures, electron tomography provides more statistically significant information for these systems.[23-26] From the reconstructed volume a 2D slice can be obtained at different orientations and depths in the volume, allowing a precise analysis of the nanoscale structure and its assembly/organization. A variety of imaging modes can be used to acquire projections for tomographic reconstruction.[27] However, due to the crystalline nature of the core-shell nanoparticles, bright-field (BF)-TEM images maybe complicated by Fresnel contrast, bend contours or thickness fringes and could lead to artifacts in the 3D reconstruction.[28] HAADF-STEM images have minimal diffraction or phase contrast, conform much better to the projection requirement and are, therefore, ideally suited for tomographic applications.[20, 27-29]

Furthermore, the data obtained from this 3D method provide precise and direct information on the nanometrology of the core-shell nanostructure and can be used as input for accurate modelling and rigorous calculations of the optical properties of this nanostructure.[22]

In this work we describe the use of HAADF-STEM electron tomography to characterize Au@Ag core-shell nanostructures, a method which, combined with electrodynamics calculations using the Discrete Dipole Approximation (DDA), provide precise and direct information on the nanometrology of the nanostructure with an appropriate calculation scheme of the optical properties.

Results and discussion

3D tomographic characterization of Au@Ag core shell nanopartidcles.

Figure 1 shows examples from a tomographic tilt series of high-angle annular dark field (HAADF-STEM) images of an agglomerate of Au@Ag core-shell nanoparticles. The images show in an intuitively clear way that the particles have core–shell structures because the intensity is lower in the shell region (due to lower Z: (47)Ag) and higher in a much more spatially compact area located at the centre of the nanoparticles (due to higher Z: (79)Au). The uniform intensity distribution observed in the shell region suggests a homogeneous chemical distribution (see Figure 1c). Indeed, HAADF-STEM image simulations performed by Perez-Tijerina and co-workers for similar model systems are in a good agreement with the proposed core-shell structure.[14]

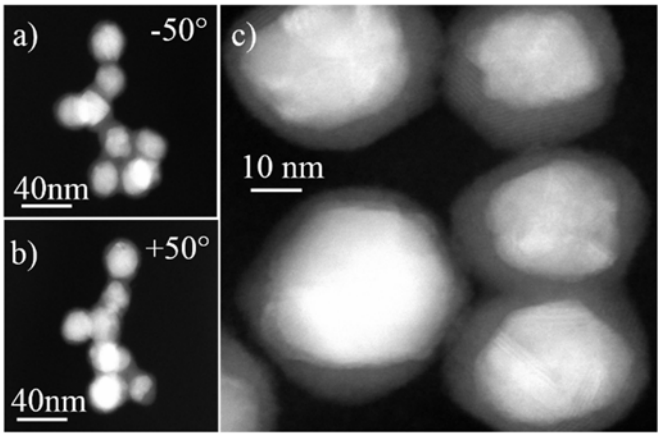

Figure 1. The STEM HAADF (Z-contrast) imaging mode reveals the core–shell structure due to the lower intensity in the shell region (lower Z: Ag) and higher in a much more spatially compact area located at the centre of the nanoparticles (higher Z: Au). Examples of images from the tilt series are shown in a) and b). A higher magnification image is shown in c).

Initial observations of the HAADF-STEM images indicate that the core-shell agglomerate is composed of Au cores, which contain a number of defects (probably twins), encompassed by a polycrystalline Ag shell; the shell appears to be slightly thicker for smaller cores and its thickness appears more anisotropic for irregular larger cores.

The resulting 3D reconstruction is presented in Figure 2 and a corresponding movie is shown in the Supporting Information. For the tomographic reconstruction showed in Figure 2a, red surface corresponds to the Au core and the yellow corresponds to the Ag shell. In order to enhance the visualization of the core-shell nanostructure the yellow surface render is shown with some level of transparency. The reconstructed volume confirms that the Ag shells are covering completely the Au cores.

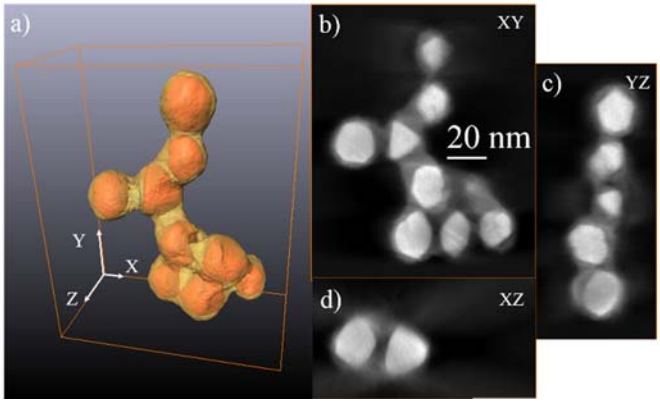

Figure 2. Tomographic reconstruction of an agglomerate of Au@Ag core-shell nanoparticles. a) Surface rendered visualization with Au cores in red and Ag Shell in yellow with some degree of transparency. b-d) Corresponding orthoslices for XY, XZ and YZ planes, respectively, of the reconstructed volume revealing the Ag shell thickness in cross-section and the Au core.

The three central orthogonal slices through the reconstructed volume, shown in Figures 2b-d, illustrate that whilst the Au cores are faceted nanocrystallites, the Ag shells have mainly round shapes.

A close inspection of the images within the tilt series show that some Au nanoparticles (NPs) contain diffraction contrast indicative of twinning. In fact, for the size of these Au NPs,

multiply twinned particles are expected.[30] Although diffraction contrast should be minimized to reduce the possible artifacts in the reconstructions,[28] in this case it allows us to recognize the presence of twins without unduly affecting the quality of the reconstructed outer morphology (i.e. faceting) (see Figure S1 in Supplementary Information).

From the reconstruction shown in Figure 2, it is clear that the Au cores are facetted. From the 3D morphology of the cores, and the fact that many twin boundaries seen are parallel to the outer face, we can say the facetted planes are predominantly {111}. If we focus on the central nanoparticle, as shown in Figure 3, an interesting structural feature has been observed in that the core has a clear tetrahedral morphology. Moreover there appears to be a tetrahedral-like growth of branches where each branch has its origin on a {111}-type plane of this central nanoparticle.

As known in the literature, the shape of metallic shells depends strongly on both the shape of the metallic cores and on the epitaxial growth that it is known to be favorable when the lattice mismatch between cores and shells is less than 5%. In this sense, the tetrahedral-like growth of the branches from the Au central nanoparticle can be explained in terms of the truncated tetrahedron morphology of that central nanoparticle, dominated by {111}-type planes, and the negligibly small lattice mismatch (0.2%) between Au and Ag[11, 12] Finally, the occurrence of a very thick Ag layer surrounding this central nanoparticle may be explained in terms of a fast growth rate of the {111} facets, as has been described for similar Au@Pd core-shell nanostructures.[31]

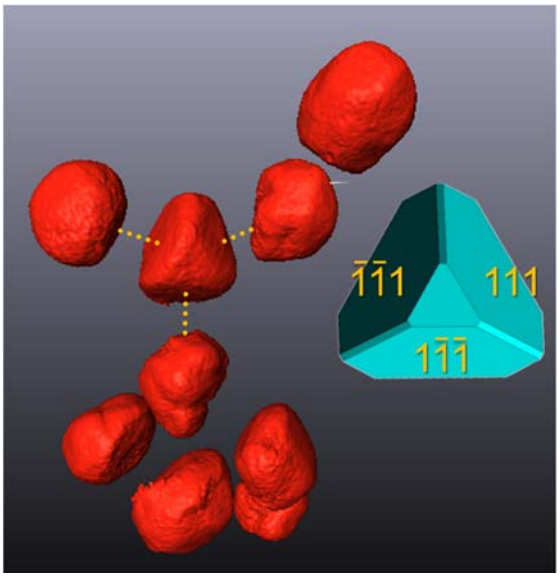

Figure 3. Tomographic reconstruction for the Au-core nanoparticles showing the agglomerate's 'branches' based on a tetrahedral-like growth starting from a central Au nanoparticle dominated by {111} facets, indexed as a truncated tetrahedral particle (model shown).

In addition, to determine quantitatively the 3D morphology of the core and the shells, surface renderings were obtained by a segmentation procedure from the reconstructed volume as described in more details in Supporting Information. Figure 4 shows the tomographic reconstruction in which a sub-volume near the uppermost nanoparticle has been highlighted. A nanoscale quantitative analysis has been performed over the selected nanoparticles which have been cut to reveal the Ag shell thickness in cross-section and the Au interior. Similar analysis has been performed for each nanoparticle within the cluster.

The 3D measurements on the uppermost particle reveal an average core diameter of ~23 nm with a corresponding average shell thickness of ~ 2.3 nm. In general, our studies reveal that the larger the core, the thinner the shell.

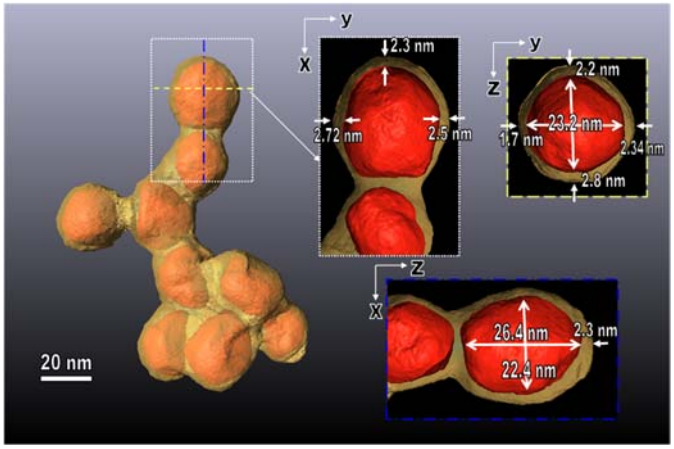

Figure 4. Orthogonal views of the uppermost nanoparticle showed in the corresponding tomographic reconstruction. The particle has been cut to reveal the Ag shell thickness in cross-section and the Au core.

Plasmonic properties of Au@Ag core shell nanoparticles

The capability of electron tomography to give such a detailed morphological information about the size and shape of the Au core as well as the Ag shell, opens up the question on the sensitivity of the far and near field optical properties of these type of hybrid nanostructures to their size and shape for particles having the same equivalent volumes of the core and the shell. For such a purpose we will focus on the central nanoparticle shown in Figure 3 whose core morphology can be interpreted as an irregular truncated tetrahedron nanoparticle. In this case we will compare the optical properties of an ideal model for the real particle consisting a truncated tetrahedral core, such as shown in Figure 3, to the more accurate NP reconstruction corresponding to the same NP core but with rounded edges. We will denote the first as irregular polyhedral core (IPC) while the second one by reconstructed irregular polyhedral core (RIPC). For reference we will also compute the optical properties of an equivalent volume spherical core (SC).

Then we will address the question of how the optical properties of these three NP cores are affected when these cores are capped with a Ag shell, all of them having the same equivalent volume (the average shell thickness is around 2.25 nm, 2.23. and 2.3 for the IPC, RIPC and SC nanoparticles respectively).

The optical properties presented here, were calculated using the discrete dipole approximation (DDA). Further details about the basics of these electrodynamics calculations and about the adaptive DDA method can be found in elsewhere.[22] The optical response should also be dependent on the dielectric environment. At this stage we have performed the calculations in nanoparticles in a homogeneous dielectric environment corresponding to water. The actual dimensions of the Au core used in the electrodynamics simulations are shown in Figure S2. The dataset for the NPs electrodynamics calculations entailed ~110000 and ~210000 dipoles for the core and for the core-shell respectively (with 0.37 nm inter-dipole distance).

Far field optical properties. Figure 5 compares the extinction spectra of the three above mentioned NPs, showing in solid lines the spectra of each core-shell NPs and in dashed lines the spectra of the Au NPs core. The first feature to be noticed is that the peak positions of the extinction spectra of respective Au cores are located at 525, 553 and 603nm, for the SC, RIPC and IPC shapes respectively. By adding a ~2.3 nm shell of Ag to these Au NPs cores give rise, as expected, to a blue shift of the localized surface plasmon resonance (LSPR). The peak positions of the LSPR for the Au@Ag core-shell NPs are located at 477, 503 and 527nm by adding the same equivalent volume shell to the Au SC, RIPC and IPC, respectively. In general this shift is around the same value 48nm, 50nm for the SC and RIPC shapes while it is significantly larger, 76nm, for the IPC (sphere, reconstructed polyhedral and idealized polyhedral NP respectively).
This result is in contrast with previous results obtained for regular nearly spherical core-shell NPs that highlights that the main feature that controls the peak position of the LSPR is dependent only on the volume fraction (V_{core}/V_{shell}).[24] The present simulation highlights the importance of having a detailed and precise morphological characterization since a slight variation in the shape of the NP core (by rounding the NP edges and corners) even keeping the same volume fraction give rise to a significant change on the far field optical behavior.
The above analysis can be generalized to the other NP shapes obtained in the present work, and highlights the importance of having a complete and precise 3D morphological characterization if a rigorous correlation between theory and experiments is needed as is the case of measuring the optical properties at the single NP level.

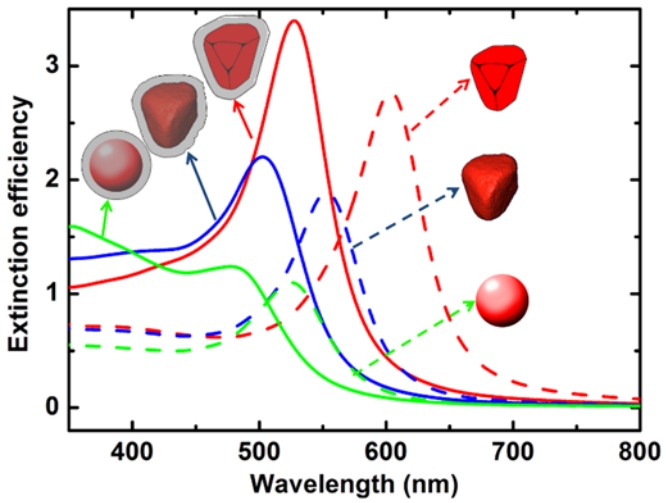

Figure 5. Extinction spectra of different equivalent volume Au cores for SC dashed green dashed lines), RICP (blue dashed line) and IPC (red dashed line) and the respective Au@Ag core-shell (solid lines with the same respective color). The SC shape diameter is 16.6nm. The details of the 3D tomographic reconstructions are indicated in Figure S2 in the supporting information. In all the cases the shell volume is the same with a ~2.3 nm average Ag shell thickness.

Near field optical properties. Let us now analyze the near field optical properties which are of great importance for instance for Raman enhanced spectroscopies such as surface enhanced Raman scattering (SERS) or tip enhanced Raman scattering (TERS). In the so called E^4 approximation the magnitude of the SERS or TERS enhancement in a given point $\underline{i}$ around the NP surface is given by the fourth power of the ratio between the electric field E in the i^{th} point and the incident electromagnetic field E_0, i.e. $(E/E_0)^4$ at the incident irradiation wavelength. This enhancement is for anisotropic NPs, and is highly dependent on the polarization direction of the incident light.
The variation of the so called enhancement factor $(E/E_0)^2$ around the different nanoparticles is depicted in Figure 6b-g for RIPC, IPC and SC shapes as well as for the respective core-shell nanostructures. In order to make a quantitative comparison, in Figure 6a we show in a color scale the variation of the SERS enhancement ($\log (E/E_0)^4$) from the surface of the NP (where the enhancement is maximum) along the direction denoted by the colored arrows in Figures 6b, 6d and 6f, respectively, for the three different Au NP cores as well for the respective core-shell NPs.
Two features deserve to be remarked. First, the maximum enhancement at the NP surface does not change significantly by adding a Ag shell to the respective gold NP core, i.e. the SERS enhancement starts at almost the same value for the core and core-shell for the three types of NP cores studied along the selected direction, and it is also independent of the morphology of the Au@Ag core-shell NP. The core shell nanoparticles depict a significantly slower rate of decay (see solid lines in Figure 6) with respect to the bare Au core NP (dashed lines in Figure 6). Second, the SERS enhancement close to the NP is highly dependent on the fine details of the NP morphology as there are orders of magnitude of difference between the idealized polyhedral NP ($\sim 5\times10^4$) and the spherical NP ($\sim 4\times10^2$). These is not a minor issue when considering possible applications of core-shell NP for SERS/TERS spectroscopies, for example at the single NP level the maximum SERS enhancement should be almost 10^2 times greater for the idealized polyhedral core-shell NP than for the equivolume spherical one. The real RIPC with a Ag shell has a maximum SERS enhancement of around 3×10^3 at the NP surface which is a value in between the above mentioned values. This result demonstrate that a slight variation of the morphology of the core by rounding the vertexes and corners have significant implications in the SERS response.
Let us now focus our attention to the RIPC and IPC shapes and its near field optical properties. The influence of adding a 2.3 nm Ag shell give rise only to a subtle change in the SERS enhancement, however a closer inspection of the SERS enhancement decay curves for each shape reveals that both curves crosses at a given distance, being in both cases the SERS enhancement greater for the Au@Ag core-shell NPs at long distances in comparison with the bare Au NP core.
The effect of adding a silver shell for to RIPC NP open up two questions: First if there is any change in the localized surface plasmon mode being excited and second what is the relation between the enhancement and the excitation wavelength for both the bare core and the core-shell NP. The vector plot shows in Figure 7a,b the components of the electric field along the middle plane of the real NP for excitation at a wavelength of 500 and 555 nm for the Au core and the Au@Ag core-shell NP respectively. The direction of electric field vectors projected in the xy plane (see Figure S3 in Supporting Information) around the NP indicates that at both wavelengths a dipole mode is excited. A comparison between the distribution of the enhancement factor $(E/E_0)^2$ for the Au NP core and the corresponding core-shell NPs is also depicted in Figure 7a,b.

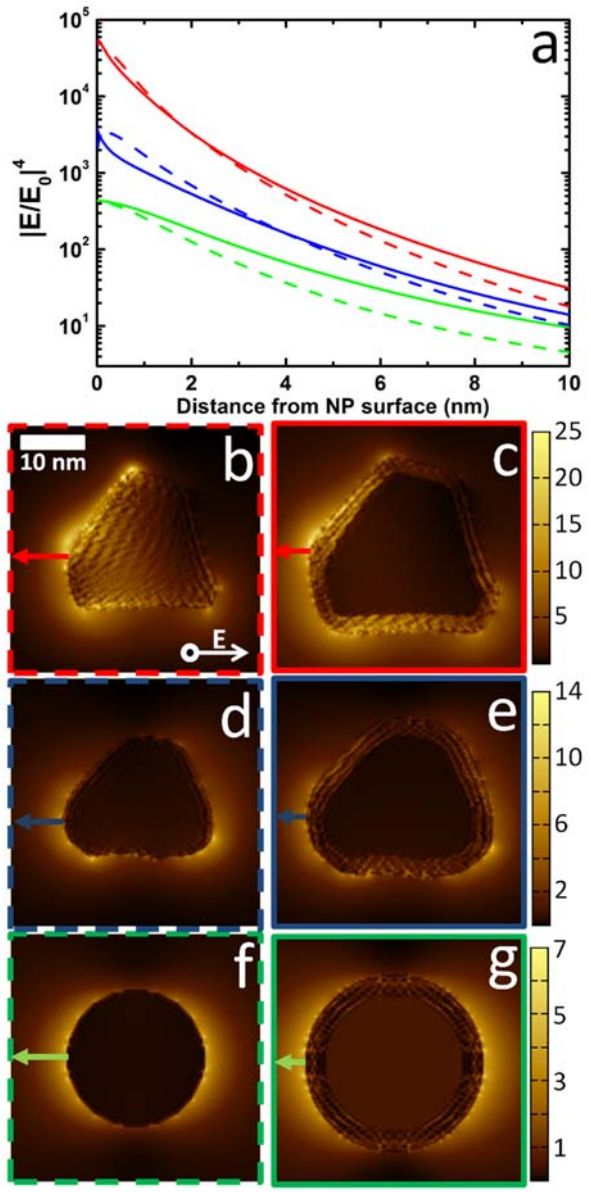

Figure 6. Panel a: Decay curves from the NP surface of the square of the EFEF factor along the direction indicated by colored arrow in panels b-g, for the IPC, RIPC and SC shapes (dashed red, blue and green lines respectively) and the decay curves of the respective core shell Ag@Au NPs for the same shapes (solid red, blue and green lines). Panels b, d and f depict the electric field enhancement (E/E_0) for the IPC, RIPC and SC shapes while panels c,e and g shows the respective distribution of the electric field enhancement (E/E_0) produced by adding a silver shell to each Au NP core. All the calculations were performed with the same incident polarization as indicated in the bottom of panel b

An answer to the second question is given in Figure 7c where we compare the fourth power of the field enhancement spectra of the Au core and Au@Ag core-shell NP as a function of the incident wavelength. The optimum SERS response, corresponding to the maximum of each of the curves depicted in Figure 7c, is around λ=569nm for the core NP while the optimum excitation wavelength is at a relatively lower value, λ=521nm, for the respective core-shell. Both maxima are red shifted from their extinction maximum (Δλ~16nm). There is not any significant difference between the SERS enhancement maximum and they can be considered almost equivalent (2.5 10^4 and 3 10^4 for the IRP core and core-shell respectively). However as the maxima are shifted, at short wavelengths the Au@Ag core-shell NPs give rise to a better SERS performance, being the enhancement greater for the bare Au core for wavelengths longer than 540nm.

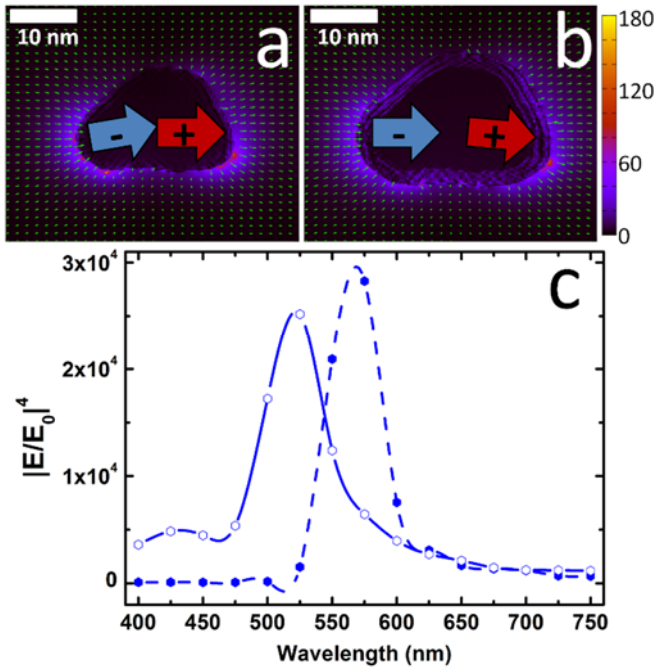

Figure 7. a,b) Comparison between the electromagnetic field enhancement factor between the RIPC Au shape (panel a) and the corresponding Au@Ag nanoparticle with a 2.3 nm silver shell (panel b) at λ=555nm and λ=500nm, respectively. c) Variation of the square of the electric field enhancement factor (EFEF) as a function of the wavelength for the RIPC Au shape (dashed blue lines) and the corresponding Au@Ag nanoparticle with a 2.3 nm silver shell (solid blue line).

Experimental

The Au@Ag core-shell nanoparticles were synthesized using a two-step strategy: in the first step Au nanoparticles were generated using the Turkevich method.[32] Briefly, 95mL of a 2.5x10-4 M $HAuCl_4$ solution was heated at the boiling point temperature under vigorous stirring, then 5 mL of a 1% sodium citrate solution was added and the reactants were allowed to react during 45 minutes. The dispersion has the characteristic ruby red colour of spherical Au nanoparticles dispersions. In the second step Ag^+ was reduced onto the Au nanoparticle surface, accomplished by adding to the Au NP dispersion 40 mL of $AgNO_3$ (2,.5x10^{-4}M) and sodium citrate (1%).

The core-shell nanoparticles were dispersed onto holey carbon-supported Cu TEM grids. Electron tomography was performed on an FEI Tecnai F20 electron microscope at an accelerating voltage of 200 kV. The tilt-series was acquired in HAADF-STEM mode (inner angle of detector = 35 mrad) using a Fischione ultra-high-tilt tomography holder in the tilt range of -74º to +66º, with images recorded every 2º and with a 0.20 nm resolution. Many TEM parameters were controlled during the acquisition of the tilt series of projections: defocus, image shift, specimen tilt, and the condenser lens astigmatism. Once the acquisition of the tilt series was completed, images were spatially aligned by a cross-correlation algorithm using Inspect3D software, and 3D reconstructions were achieved using a simultaneous iterative reconstruction algorithm (SIRT) of

consecutive 2D slices. Visualization was performed using AMIRA 3.1.
The optical properties presented here were calculated using the Discrete Dipole Approximation (DDA).[33]

Conclusions

In summary, we have demonstrated a comprehensive approach for three-dimensional nanometrology of Au@Ag core-shell nanostructures by HAADF-STEM based electron tomography. The information yielded by this method provides morphological and structural features of this kind of complex nanostructures which are potentially key parameters for electrodynamic simulations of their optical properties. Our results reveal the great potential of this 3D technique for various applications regarding the nanometrological characterization of all kinds of complex core-shell structured materials, particularly nanoparticles. Particularly we have demonstrated the importance of having a precise and detailed morphological reconstruction of the core, since its morphological features controls the near and far field optical properties. We have illustrated this fact by simulating the effect of adding an equivalent volume silver shell to equivalent volumes Au cores of different morphologies: sphere, idealized polyhedral, and the tomography reconstructed anisotropic NP whose shape has been precisely characterized using HAADF-STEM. It has been found that the addition of a thin silver shell give rise to blue shift of the LSPR for the three examples analyzed, being more significant for the NP having sharper edges and corners. The effect of rounding the corners give rise to a blue shift similar to that of a sphere.
The near field simulations for the different nanoparticle shapes show that the magnitude of the SERS enhancement at the peak positions of the extinction spectra is highly dependent of the detailed morphology of the Au core. There is an almost one order of magnitude difference in the SERS enhancements for the equivolume cores (being around 10^2, 10^3 and 10^4 for the SC, RIPC and IPC shapes, respectively). The effect of adding a silver shell does not give rise to a significant difference in the decay of the SERS enhancement at short distances from the surfaces. At larger distances the differences between these decays are more pronounced for the SC shape, followed by the IPC and RIPC shapes. Analysing the maximum SERS enhancement as a function of the wavelength produced by adding a silver shell to the RIPC show that the optimum wavelength blue shifted with respect to the core (it shifts from 569 to 521 nm) and that in both cases a dipole mode is excited. However as the maxima are shifted, at short wavelengths the Au@Ag core-shell NPs give rise to a better SERS performance, being the enhancement greater for the bare Au core for wavelengths longer than 540nm.

Acknowledgements

JCH acknowledges support from the Ramon y Cajal Fellowships Program of MINECO (RYC-2012-10004). The research leading to these results has received funding from the European Research Council under the European Union's Seventh Framework Program (No. FP7/2007-2013)/ERC Grant Agreement No. 291522-3DIMAGE; CD acknowledges funding from the ERC under Grant Agreement No. 259619 PHOTO EM. JCHG, CD and PAM also acknowledges funding from the European Union's Seventh Framework Program under a contract for an Integrated Infrastructure Initiative (Reference No. 312483-ESTEEM2). H.E. Butt is thanked for the preparation of the samples. MSM thanks partial financial support of CONICET (Argentina). LAP and EAC acknowledges financial support from CONICET, SECYT-UNC, and ANPCyT, Argentina.

Notes and references

[a] Departamento de Ciencia de los Materiales, Ingeniería Metalúrgica y Química Inorgánica, Facultad de Ciencias, Universidad de Cádiz, Río San Pedro s/n, Puerto Real, 11510, Spain.
[b] Centro Atómico Bariloche, San Carlos de Bariloche, 8400, Argentina.
[c] Department of Materials Science and Metallurgy, University of Cambridge, Pembroke Street, Cambridge, CB2 3QZ, United Kingdom.
[d] INFIQC. Centro Laser de Ciencias Moleculares, Dpto. de Físico Química, Facultad de Ciencias Químicas, Universidad Nacional de Córdoba, Córdoba, 5000, Argentina.
Electronic Supplementary Information (ESI) available: [3D reconstruction movie and supplementary figures]. See DOI: 10.1039/b000000x/

1. Y. Cao, J. Rongchao and C. A. Mirkin, *J. Am. Chem. Soc.*, 2001, **123**, 7961-7962.
2. J. Zhu, Y. Wang, L. Huang and Y. Lu, *Phys. Lett. A*, 2004, **323**, 455-459.
3. H. Zeng, J. Li, Z. L. Wang, J. P. Liu and S. Sun, *Nano Letters*, 2004, **4**, 187-190.
4. J. K. Edwards, B. Solsona, P. Landon, A. F. Carley, A. Herzing, M. Watanabe, C. J. Kiely and G. J. Hutchings, *J. Mater. Chem.*, 2005, **15**, 4595-4600.
5. G. Schmid, H. West, J.-O. Malm, J.-O. Bovin and C. Grenthe, *Chem. - Eur. J.*, 1996, **2**, 1099-1103.
6. R. Ferrando, J. Jellinek and R. L. Johnston, *Chem. Rev. (Washington, DC, U. S.)*, 2008, **108**, 845-910.
7. J. M. Thomas, B. F. G. Johnson, R. Raja, G. Sankar and P. A. Midgley, *Acc. Chem. Res.*, 2002, **36**, 20-30.
8. S. J. Oldenburg, R. D. Averitt, S. L. Westcott and N. J. Halas, *Chem. Phys. Lett.*, 1998, **288**, 243-247.
9. L. M. Liz-Marzán, *Langmuir*, 2005, **22**, 32-41.
10. B. Rodriguez-Gonzalez, A. Burrows, M. Watanabe, C. J. Kiely and L. M. Liz Marzan, *J. Mater. Chem.*, 2005, **15**, 1755-1759.
11. M. Tsuji, R. Matsuo, P. Jiang, N. Miyamae, D. Ueyama, M. Nishio, S. Hikino, H. Kumagae, K. S. N. Kamarudin and X.-L. Tang, *Cryst. Growth Des.*, 2008, **8**, 2528-2536.
12. M. Tsuji, D. Yamaguchi, M. Matsunaga and M. J. Alam, *Cryst. Growth Des.*, 2010, **10**, 5129-5135.
13. A. Sánchez-Iglesias, E. Carbó-Argibay, A. Glaria, B. Rodríguez-González, J. Pérez-Juste, I. Pastoriza-Santos and L. M. Liz-Marzán, *Chem. - Eur. J.*, **16**, 5558-5563.
14. E. Perez-Tijerina, M. G. Pinilla, S. Mejia-Rosales, U. Ortiz-Mendez, A. Torres and M. Jose-Yacaman, *Faraday Discuss.*, 2008, **138**, 353-362.
15. I. Srnová-Sloufová, F. Lednický, A. Gemperle and J. Gemperlová, *Langmuir*, 2000, **16**, 9928-9935.
16. S. Pyne, P. Sarkar, S. Basu, G. P. Sahoo, D. K. Bhui, H. Bar and A. Misra, *J. Nanopart. Res.*, 2011, **13**, 1759-1767.
17. S. J. Pennycook and L. A. Boatner, *Nature*, 1988, **336**, 565-567.
18. S. J. Pennycook, D. E. Jesson, A. J. McGibbon and P. D. Nellist, *J Electron Microsc (Tokyo)*, 1996, **45**, 36-43.

19. D. Garcia-Gutierrez, C. Gutierrez-Wing, M. Miki-Yoshida and M. José-Yacaman, *Appl. Phys. A: Mater. Sci. Process.*, 2004, **79**, 481-487.
20. P. A. Midgley and M. Weyland, *Ultramicroscopy*, 2003, **96**, 413-431.
21. I. Arslan, J. R. Tong and P. A. Midgley, *Ultramicroscopy*, 2006, **106**, 994-1000.
22. E. M. Perassi, J. C. Hernandez-Garrido, M. S. Moreno, E. R. Encina, E. A. Coronado and P. A. Midgley, *Nano Letters*, 2010, **10**, 2097-2104.
23. S. Bals, M. Casavola, M. A. van Huis, S. Van Aert, K. J. Batenburg, G. Van Tendeloo and D. l. Vanmaekelbergh, *Nano Letters*, 2011, **11**, 3420-3424.
24. L. Chuntonov, M. Bar-Sadan, L. Houben and G. Haran, *Nano Letters*, 2012, **12**, 145-150.
25. S. Gómez-Graña, B. Goris, T. Altantzis, C. Fernández-López, E. Carbó-Argibay, A. Guerrero-Martínez, N. Almora-Barrios, N. López, I. Pastoriza-Santos, J. Pérez-Juste, S. Bals, G. Van Tendeloo and L. M. Liz-Marzán, *The Journal of Physical Chemistry Letters*, 2013, **4**, 2209-2216.
26. B. Goris, A. De Backer, S. Van Aert, S. Gómez-Graña, L. M. Liz-Marzán, G. Van Tendeloo and S. Bals, *Nano Letters*, 2013, **13**, 4236-4241.
27. P. A. Midgley and R. E. Dunin-Borkowski, *Nat. Mater.*, 2009, **8**, 271-280.
28. P. W. Hawkes, in *Electron Tomography: Three dimensional Imaging with the Transmission Electron*, ed. J. Frank, Plenum Press New York, London, 1992.
29. J. C. González, J. C. Hernández, M. López-Haro, E. del Río, J. J. Delgado, A. B. Hungría, S. Trasobares, S. Bernal, P. A. Midgley and J. J. Calvino, *Angew. Chem., Int. Ed.*, 2009, **48**, 5313-5315.
30. L. C. Gontard, R. E. Dunin-Borkowski, M. H. Gass, A. L. Bleloch and D. Ozkaya, *J. Electron Microsc.*, 2009, **58**, 167-174.
31. F.-R. Fan, D.-Y. Liu, Y.-F. Wu, S. Duan, Z.-X. Xie, Z.-Y. Jiang and Z.-Q. Tian, *J. Am. Chem. Soc.*, 2008, **130**, 6949-6951.
32. J. Turkevich, P. C. Stevenson and J. Hillier, *Discuss. Faraday. Soc.*, 1951, 55-&.
33. F. Le, D. W. Brandl, Y. A. Urzhumov, H. Wang, J. Kundu, N. J. Halas, J. Aizpurua and P. Nordlander, *ACS Nano*, 2008, **2**, 707-718.